EarthArXiv Coversheet

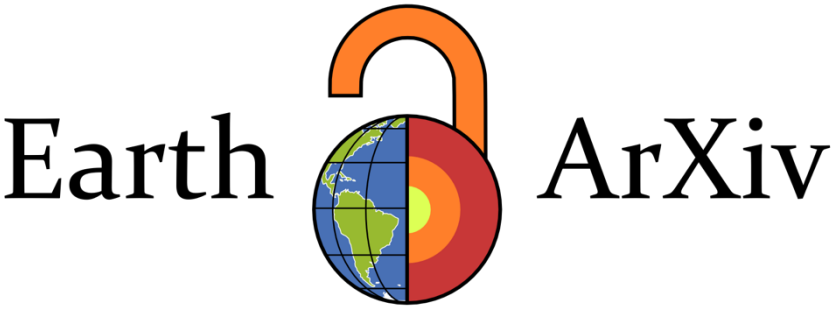
Dominik Nommensen[1], Jimmy Daynac[2], Andrew Gunn[1,*]

[1]School of Earth, Atmosphere and Environment, Monash University, Clayton, Victoria 3800, Australia

[2]Géosciences Rennes, UMR CNRS 6118, OSUR, Université Rennes 1, 35042 Rennes Cedex, France

[*]a.gunn@monash.edu

This is a non-peer-reviewed preprint submitted to EarthArXiv



Inferred vegetation during Australia's dune whorl formation

Dominik Nommensen[1], Jimmy Daynac[2], Andrew Gunn[1,*]

[1]School of Earth, Atmosphere and Environment, Monash University, Clayton, Victoria 3800, Australia

[2]Géosciences Rennes, UMR CNRS 6118, OSUR, Université Rennes 1, 35042 Rennes Cedex, France

[*]a.gunn@monash.edu

Abstract

Australia's vegetated linear dune crests are oriented in an anticlockwise whorl covering over a third of the continent. The mismatch between its crest orientations and modern sand-flux directions has been interpreted as evidence of a northward wind shift during the Last Glacial Maximum. However, this interpretation implicitly assumes constant vegetation cover via the threshold wind speed for sand transport. Here we show that modern winds can reproduce the whorl across much of the continent if the threshold speed varies spatially. We combine a continental map of crest orientation with a sand-flux model driven by reanalysis winds. The thresholds required to match observed orientations imply lower vegetation cover than the contemporary minimum in many regions, and less spatial contrast across the continent, indicating whorl formation occurred during more arid climates within the glacial cycles. Plausible changes in vegetation alter dune orientation as much as the postulated wind shift. Across-crest observed slope asymmetry and predicted sand flux both agree to imply increasing vegetation as dunes reoriented until they became immobile. Our results do not exclude interglacial wind variability but show that vegetation variability sufficiently reconciles the whorl with modern winds and therefore vegetation should be considered when inferring past climate from dune orientation.

Introduction

Dunes are archives of past wind systems and climates in arid and inaccessible regions[1]. In Australia, vegetated dune fields form the continent's largest landform pattern[2] and their linear crests trace an anticlockwise whorl around the interior[2–7] which broadly follows the modern resultant sand-moving wind[8,9]. Departures from this direction have led to interpretations that their formative wind system was shifted northward relative to present, by 1–1.5° of latitude in the western Simpson Desert[10] or by more than 5° in the south[11], and occurred during glacial phases such as the Last Glacial Maximum (LGM), implying dune formation during these periods. However, the corpus of optically stimulated luminescence (OSL) ages suggests a more spatially and temporally heterogeneous formation of the dune whorl throughout the last glacial cycle, implying dunes may not have formed in a distinct period of different wind regime[12,13].

Heterogeneous dune activity could be explained by changes in vegetation cover driven by climate and fire within the last glacial cycle[13]. Modern vegetation and cyanobacterial crusts raise the threshold wind speed for sand transport so much that little sand moves and dunes remain mostly immobile[14–17]. Dunes become active only when drought or fire reduces vegetation cover, then they stabilize again as vegetation recovers[18]. Dunes therefore may have formed under lower average vegetation cover than today, yet the drift-potential calculations used to infer wind shifts from dune orientation assume a constant threshold speed for a fixed, continent-wide, bare, vegetation-free surface[9]. They are also based on a sparse wind dataset[9]. While vegetation has been invoked as a control on dune activity and shape[13,15,19], its effect on sand-flux directions, and hence on dune orientation, has not been tested against the observed Australian dune pattern at continental scale.

Across-crest slope asymmetry may be a further constraint on changing thresholds. This has been observed across Australia[5] and steeper eastern flanks in the Simpson and Strzelecki deserts have evidenced interpretations of lateral dune migration[20,21]. Partial migration over Pleistocene cores[19] could be controlled by humid and arid phases via vegetation cover. However, slope asymmetry and potential dune migration for the whole whorl remain poorly constrained by this regional evidence.

Here we combine a continental map of dune orientation and slopes with a sand-flux model driven by reanalysis winds[22], using recent advances in understanding of dune–wind interaction[1,23]. We show that the modern wind regime can reconcile the whorl through spatially varying, vegetation-modulated threshold speeds, without a northward wind shift, and that slope asymmetry is consistent with dunes reorienting as vegetation increased. These insights improve both interpretations of past climate from dunes and forecasting of dune activity in a warming climate[24].

A continental map of signed dune orientation

We derive crest lines from topography[25,26] (Methods M1–M2, Extended Data Fig. 1b–d) and assign each 0.1°×0.1° cell a mean dune orientation, signed by the upwind-facing y-junctions (Methods M3, Extended Data Fig. 1e,f). The signed orientation map (Fig. 1a) shows the anticlockwise whorl centred near 26° S. Most cells contain parallel linear dunes, but other dune types occur: parabolic dunes in the Mallee and Wiso dune fields, network dunes and mounds in the centre of the whorl, and multi-crested linear dunes in the Great Sandy Desert. Dune orientation and the distribution of dune types agree with earlier studies[2,3,27]. The areas with non-linear dunes show high dune interaction indices[28] (Methods M4, Extended Data Fig. 2a) and high circular standard deviations of crest orientation (Extended Data Fig. 2b), indicating orientation uncertainty and possible changes in boundary conditions[28,29]. Some dune types like the parabolic dunes — usually associated with a more unimodal wind regime[1] — in the Mallee or Wiso seem to match the directionality of modern sand flux[30] (the ratio of resultant drift potential and drift potential (RDP/DP);

Methods M5, Extended Data Fig. 3). However, network dunes, with the highest interaction indices, occur in the centre of the whorl whereas sand fluxes are most variable (lowest flux directionality) to the south. Spatial correlation of circular standard deviations of crest orientation (Extended Data Fig. 2b) and flux variability (1-RDP/DP; Extended Data Fig. 3) is highest for a 1.9° shift in latitude and a 0.5° shift in longitude (correlation of r = 0.2; Methods M5), supporting the northward wind shift proposed in previous studies[10,11].

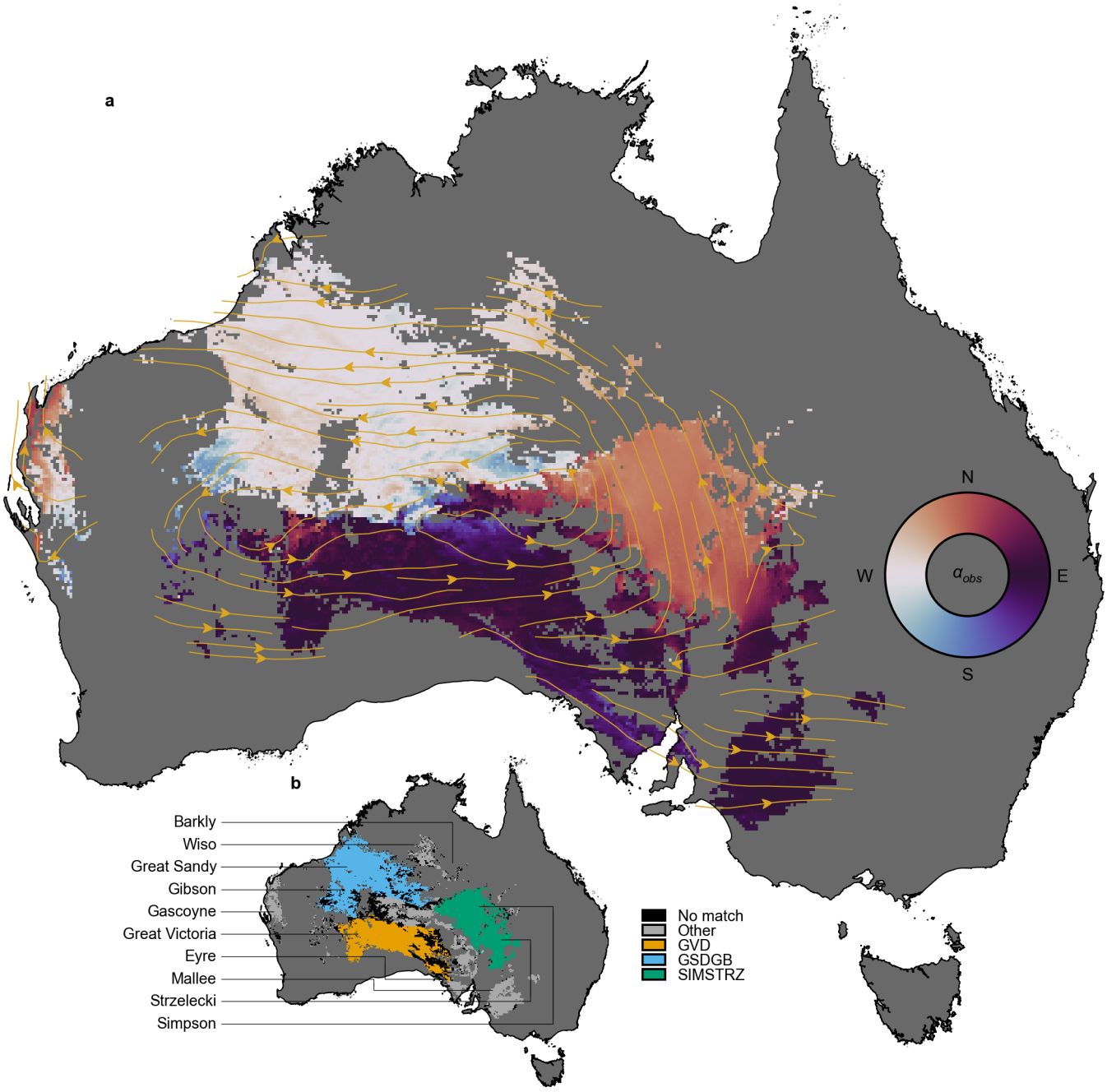


Fig. 1: Linear dune orientation across the Australian dune whorl. a, Signed dune orientation α_{obs} for each 0.1°×0.1° cell. Orientation is the circular mean of crest-line orientations in the cell, signed using the mean opening direction of dune y-junctions (Methods M1–M3; Extended Data Fig. 1b–f). Yellow spatially averaged streamlines show the broad arrangement of the whorl. **b**, Major dune fields: Great Victoria Desert (GVD) in orange, Simpson and Strzelecki deserts (SIMSTRZ) in green and Great Sandy and Gibson deserts (GSDGB) in blue, shown for cells with an optimal threshold speed $u_{*t,opt}$ (Fig. 2e). Grey: cells with $u_{*t,opt}$ outside these deserts. Black: dune-containing cells without identified $u_{*t,opt}$.

Modern winds reproduce the whorl at lower vegetation cover

Dunes are mostly inactive under the modern climate[14–17]. Using a model which relates vegetation cover to an equivalent threshold wind speed for sand transport[31] (Methods M5–M8), it is clear that even minimum modern vegetation cover's[32] (V_{mod}; Methods M6, Fig. 2a) effective threshold speeds ($u_{*t,mod}$; Methods M6, Fig. 2d) would completely suppress sand transport in parts of the whorl, for example the Mallee and parts of the Great Victoria Desert (Methods M6–M7, Extended Data Fig. 4). Elsewhere some non-persistent flux would occur, but dune activity is short-lived and limited to the crest[18]. Moreover, even if modern minimum cover was persistent it would not reproduce the observed orientations. We show

this by solving for the optimal threshold speed ($u_{*t,opt}$; Methods M8, Fig. 2e) at which the elongation mode[1,23] (α_E) matches the observed orientation of each cell (Methods M8, Extended Data Fig. 5b,c). We find a solution (non-black areas in Fig. 2) for ~82% of the whorl and translate it into an optimal vegetation cover (V_{opt}; Methods M6, Fig. 2b). V_{opt} does not represent the cover at any one time when the dunes formed. It is the cover needed to reconcile whorl orientation if formative winds resembled modern ones. Where $u_{*t,opt}$ falls below the bare-sand threshold (pink areas in Fig. 2), no vegetation cover can be inferred, but the result implies extremely low cover. We attribute this to topographic resolution (Methods M1), the quality of the underlying data and relationship between vegetation cover and threshold speed (Methods M6).

Comparing modern minimum and optimal vegetation cover ($V_{mod} - V_{opt}$; Fig. 2c) and the corresponding threshold speeds ($u_{*t,mod} - u_{*t,opt}$; Fig. 2f) shows that formative conditions deviate most where minimum modern cover is highest. Negative values (Fig. 2c,f), for example in the Great Sandy and Strzelecki deserts, do not necessarily imply that modern conditions are more arid than the optimal values suggest, because those integrate vegetation cover across the formation period rather than representing its minimum.

Modern vegetation cover correlates poorly with $u_{*t,opt}$ in the Great Victoria Desert and Great Sandy & Gibson deserts (Extended Data Fig. 6a,c). In the Simpson and Strzelecki deserts, however, the relationship is positive, although imperfect (Extended Data Fig. 6b). This suggests that vegetation cover in the most arid parts of the continent is most similar to formative conditions, whereas the margins have changed more.

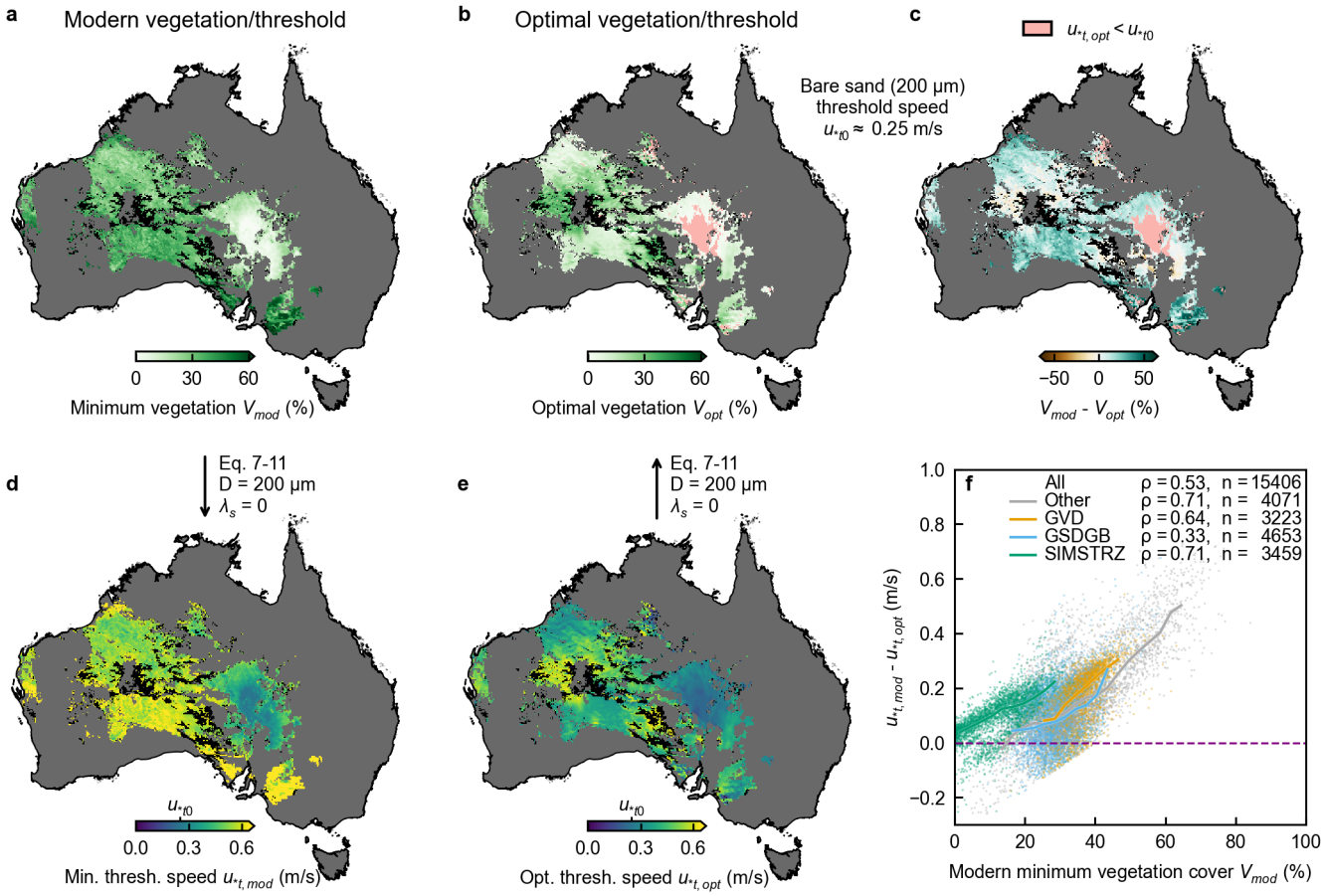


Fig. 2: Modern minimum vegetation cover and threshold speed for the Australian dune whorl. a, Fractional modern minimum total vegetation cover composite V_{mod} (photosynthetic and non-photosynthetic) for 2001 to 2025 from the Rangeland and Pasture Productivity (RaPP) dataset[32] (Methods M6). **b**, Optimal vegetation cover V_{opt} inferred from the optimal threshold speed $u_{*t,opt}$ (e) assuming continent-wide 200 µm quartz sand (Methods M6 & M8). Pink areas: $u_{*t,opt}$ below the threshold speed for bare 200 µm sand (u_{*t0}) so no vegetation cover can be inferred. **c**, Difference between modern minimum V_{mod} (a) and optimal vegetation cover V_{opt} (b). **d**, Threshold speed $u_{*t,mod}$ derived from V_{mod} (a) for 200 µm quartz sand (Methods M6). **e**, Optimal threshold speed $u_{*t,opt}$ at which the elongation mode α_E matches the observed orientation α_{obs} (Methods M8; Extended Data Fig. 5b,c). **f**, Difference between $u_{*t,mod}$ (d) and $u_{*t,opt}$ (e) against V_{mod} (a), by dune field (colours as in Fig. 1b). Lines show median trend of 3% vegetation bins (for bins >50 data points). Spearman's ρ correlations are reported for the entire whorl and for individual dune fields (ρ and n refer to scatter points). Black areas (a–e): dune-containing cells without $u_{*t,opt}$.

Slope asymmetry tracks predicted flux shifts

Dunes across the whorl show distinct slope asymmetry ΔS (Methods M3; Fig. 3c). Values are small, likely because of the resolution of the topography, but they reveal coherent regional patterns. Steeper slopes face south in the Great Victoria Desert and east across much of the Simpson Desert. In the Strzelecki Desert they face west in the south and east in the north. In the Great Sandy Desert, where dunes elongate

towards the west, the steeper side is north in the south-east and south in the north-west. Asymmetry is low and directionally mixed in the centre of the whorl, the Wiso and Gibson deserts and the Mallee, where network and parabolic dunes are present.

We hypothesize that slope asymmetry records dune reorientation (lateral migration) resulting from a change in threshold speed, with steeper depositional flanks forming on the side to which across-crest flux shifts. To test this, we calculate the change in net across-crest flux $q_{\perp}$ with threshold speed (Methods M9, Extended Data Fig. 5d–f) using observed dune orientations (Fig. 1a) and modern winds. We evaluated this at minimum modern threshold speeds (Fig. 3a,d; values from Fig. 2d) and optimal threshold speeds (Fig. 3b,e; values from Fig. 2e). If threshold-controlled changes in across-crest flux cause slope asymmetry, the two should correlate positively. At the modern minimum threshold, dunes are not in equilibrium with modern winds ($\alpha_{obs} \neq \alpha_E$), and the predicted direction of reorientation is patchy (Fig. 3a,d) and negatively correlated with the observed asymmetry (Extended Data Fig. 7). At the optimal threshold, in contrast, the predicted direction correlates positively with the observed asymmetry over large parts of the whorl (Fig. 3b,e,f). The correlation is imperfect in parts of the Great Sandy Desert, where changes in across-crest flux predict steeper slopes opposite to those observed. This may reflect non-linear dune types that affect our orientation and slope extraction (Extended Data Fig. 1&2). Alternatively, it could indicate a change in boundary conditions, such as a northward shift that reduced flux directionality (Extended Data Fig. 3, northward-shifted scenario), implying a more complex formation history.

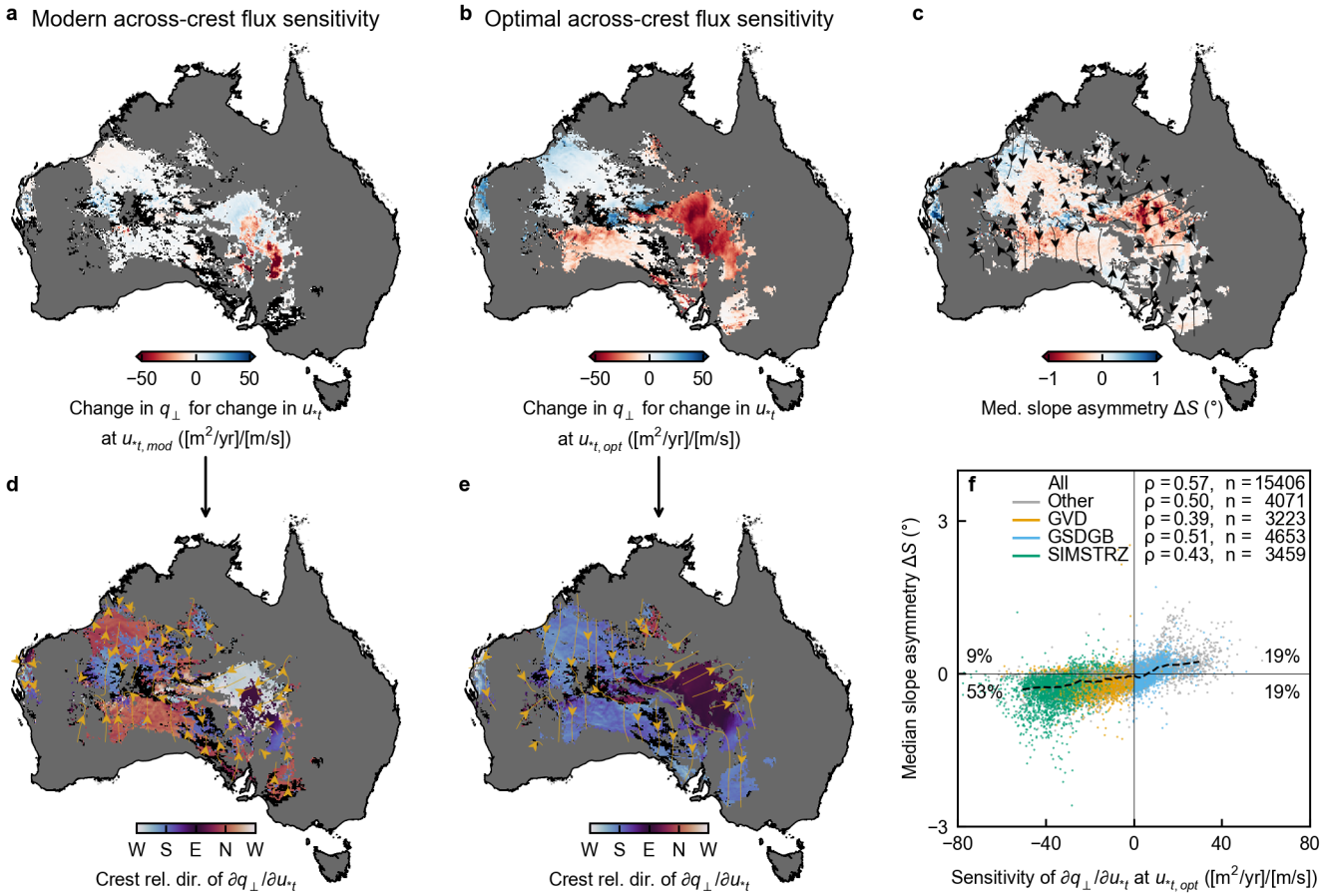


Fig. 3: Net across-crest sand flux sensitivity and slope asymmetry. a, Derivative of net across-crest sand flux $q_{\perp}$ with respect to threshold speed u_{*t} for dune orientation α_{obs} from ERA5 winds 1950 to 2025 (Methods M9). Positive and negative values indicate a shift of flux towards the left and right side of the crest (looking in α_{obs} direction; see Fig. 1a for crest orientation), respectively, for an increase in u_{*t} evaluated at $u_{*t,mod}$ (Fig. 2d). **b**, Same as in (a) but evaluated at the optimal threshold speed $u_{*t,opt}$ (Fig. 2e). **c**, Median slope asymmetry ΔS per 0.1°×0.1° cell (Methods M3). Positive and negative values indicate steeper slopes on the left and right side of the crest, respectively. **d** & **e**, Direction of change in net across-crest flux for an increase in u_{*t}, perpendicular to the crest (crest relative direction), from the derivatives in (a) and (b). **f**, Median slope asymmetry ΔS (c) over $\partial q_{\perp}/\partial u_{*t}$ for α_{obs} evaluated at $u_{*t,opt}$ (b) for each cell, by dune field (colours as in Fig. 1b). Black dashed line shows the median trend (50 equal-count quantile bins). Spearman's ρ correlations are reported for the entire whorl and for individual dune fields (ρ and n refer to scatter points). Percentages in each quadrant give the share of scatter points falling in that quadrant. If a change in net across-crest flux causes slope asymmetry we'd expect clusters in the bottom left and top right quadrant. See Extended Data Fig. 7 for this relationship evaluated at $u_{*t,mod}$ (a). Black areas (a–e): dune-containing cells without $u_{*t,opt}$. Streamlines show direction of steeper slopes (c) and direction of change of net mean across crest flux and thus potential direction of dune migration (d, e) perpendicular to α_{obs} (Fig. 1a; Methods M9).

Vegetation rivals a wind shift in setting orientation

Dune orientation depends on the distribution of sand-moving crest winds and on the threshold speed that winds must exceed. A northward shift of the wind system[10,11] would change the former, whereas vegetation changes the latter. To compare their influence, we calculate the sensitivity of the elongation mode α_E (the elongation direction of the dune) to a 1.5° latitudinal shift[10] of the wind regime (Fig. 4a) and to a 0.30 m/s change in threshold speed, equivalent to a change in vegetation cover of roughly 30% (Methods M6, Fig. 4b). Both are evaluated using the same threshold (0.29 m/s) used in earlier continental drift maps[9,10] and fixed continent-wide dune slope (Methods M10). Across most of the whorl, the change in threshold speed influences α_E more than the latitudinal shift (Fig. 4c,f). Only in the Great Sandy and Gibson deserts is α_E more sensitive to latitudinal shift. Correspondingly, the change in threshold speed, and hence in vegetation cover, required to match a 1.5° shift is modest across much of the whorl (Fig. 4d,e).

This does not imply that the modern and formative wind systems are identical. It shows that plausible changes in vegetation can alter dune orientation as much as the postulated wind shift. Unlike a shift of the entire wind system, vegetation can also vary in space and time, producing a more heterogeneous signal of dune ages and orientations.

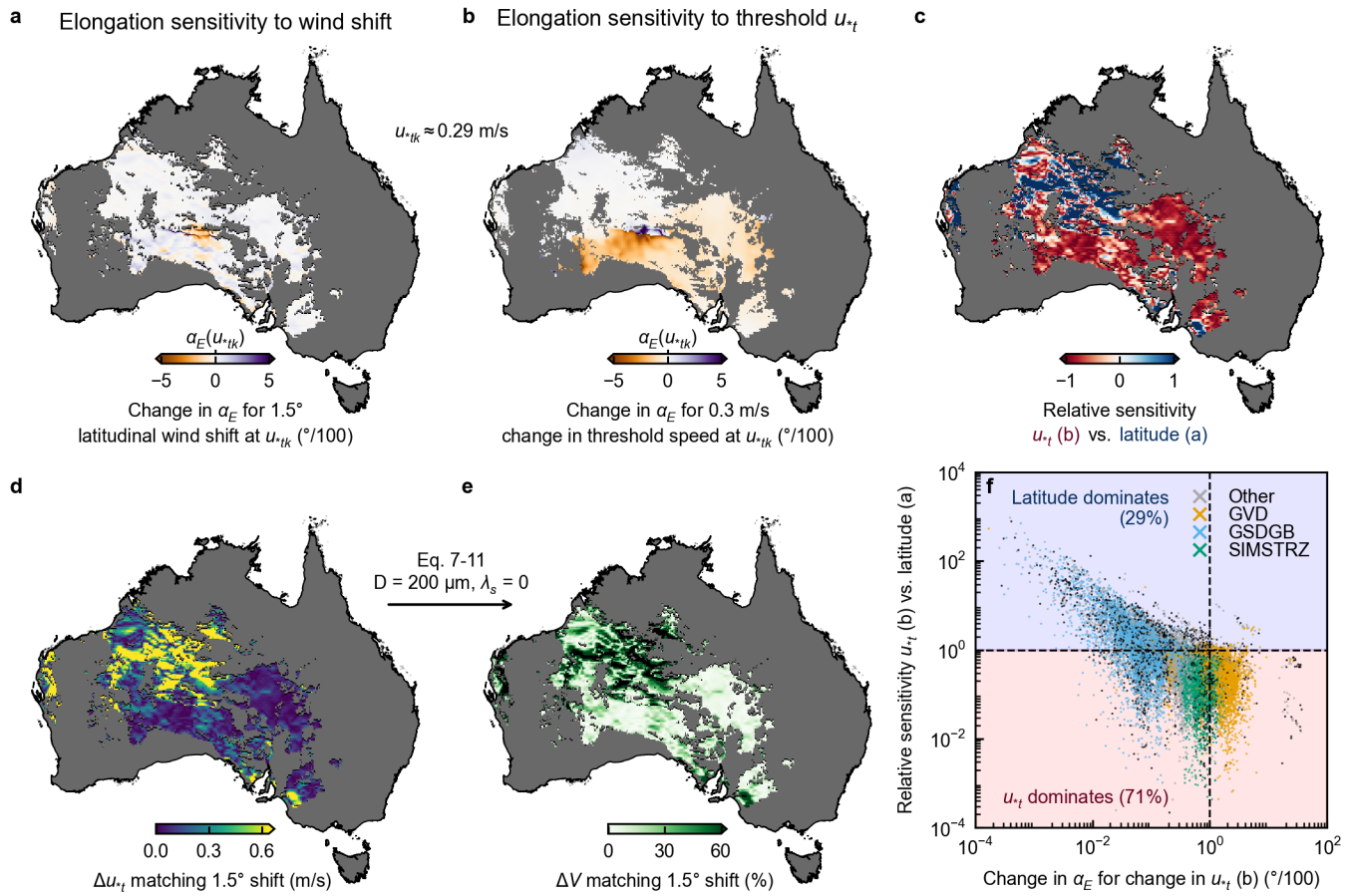


Fig. 4: Sensitivity of dune elongation direction to a latitudinal shift and to threshold speed. a, Change in the elongation mode α_E for a 1.5° latitudinal shift of the wind regime[10], at a fixed continent-wide dune slope (fixed dune aspect ratio; Methods M5), evaluated at constant threshold speed[9] u_{*tk} (Methods M10). **b**, Change in α_E for a 0.30 m/s (equivalent to a change of ~30% in vegetation cover) change in u_{*t}, evaluated at u_{*tk}. Both (a) and (b) are divided by 100 for display. **c**, Ratio of the absolute changes in (a) and (b), minus 1 (Methods M10): red indicates higher sensitivity of α_E to 0.30 m/s change in u_{*t} and blue indicates higher sensitivity of α_E to a 1.5° latitudinal wind shift. **d**, Change in u_{*t} (Δu_{*t}) required to match absolute change in α_E caused by a 1.5° latitudinal wind shift (Methods M10). **e**, Equivalent change in vegetation cover (ΔV) assuming 200 µm quartz sand (Methods M6). **f**, Relative sensitivity shown in (c) over elongation mode sensitivity to threshold speed shown in (b), by dune field (colours as in Fig. 1b).

Discussion

Vegetation as a major control on dune orientation

Our results show that the modern wind regime could form the Australian dune whorl across much of the continent if the threshold speed varies in space. The associated vegetation cover is, in many regions, lower than the modern minimum and varies less across the whorl. A northward wind shift is not the only explanation for the whorl's orientation, and plausible changes in vegetation alter dune orientation as much as the shift proposed for the western Simpson Desert (Fig. 4)[10]. Unlike a shift of the whole wind system, vegetation also varies in space and time, which offers a natural

explanation for the heterogeneous ages of dune activity[12]. Our analysis cannot settle whether dunes formed in distinct periods under a continent-wide change in wind system or through intermittent, heterogeneous activity over the last glacial cycle[12], because modern topography, winds and vegetation cannot reconstruct activity over more than 120 ka. It does, however, weaken the main argument that mismatches between dune orientation and modern sand-flux direction require different winds, both in this Australian context and generally (e.g., the Kalahari[33]).

Slope asymmetry as a record of the last reorientation

Slope asymmetry provides an independent line of evidence. Over large parts of the whorl, the direction in which across-crest flux shifts as threshold speed increases mostly agrees with the observed asymmetry at the optimal threshold (Fig. 3f), but not at the modern minimum (Extended Data Fig. 7). Earlier studies proposed that longitudinal dunes migrate laterally[20,21,34] in response, via a different mechanism, to changing vegetation cover[19]. Because dunes respond slowly to changing boundary conditions[35], one flank can steepen much faster than the whole dune can change orientation. During sparsely vegetated phases, dunes could elongate in equilibrium with the elongation mode. As vegetation increased and the elongation mode rotated, dunes could have reoriented, depositing sand on the new net lee side, until vegetation left them effectively immobile. Slope asymmetry would then record the last, possibly incomplete, adjustment towards a new equilibrium, and the same process could explain why dunes move around their Pleistocene cores[19]. This mechanism could apply for other controls on threshold (e.g., coarsening sand supply).

Where changes in wind regime may still matter

The agreement is not uniform. In the Great Sandy and Gibson deserts, a 1.5° latitudinal shift outweighs a plausible change in threshold speed (Fig. 4c,f). In parts of the Great Sandy Desert, slope asymmetry is also opposite to the predicted flux shift (Fig. 3c,f). The north-central whorl is also where complex dune types with high interaction density are concentrated (Extended Data Fig. 2) and where a northward shift would produce the strongest change in flux directionality (Extended Data Fig. 3). Together, these patterns make it the part of the whorl where a change in wind regime is most plausible, although ephemeral lakes and creeks, sand supply, topographic barriers and underlying topography may also contribute[28,36]. Elongation stability at the optimal threshold does not support formation by elongation across large parts of the whorl either (Extended Data Fig. 8)[1,37]. We therefore do not argue that vegetation alone set dune orientation. The whorl more likely records an interplay of vegetation, wind regime and local boundary conditions.

Our estimates rest on several assumptions: a single grain size (200 μm), no soil moisture, roughness or crust effects beyond what is incorporated in the vegetation-threshold model, 30-m resolution topography, and 10-m high reanalysis winds interpolated from 0.25° to 0.1° resolution. The optimal vegetation cover is therefore a relative, time-integrated measure of how open the surface was, not a reliable absolute palaeo-cover. Even so, dune orientation in vegetated deserts is a joint signal of wind and surface threshold, and palaeowind inferences from dune orientation need to account for both. The same applies to the future: changes in vegetation cover under a warming climate[24] may steer dune orientation as much as changes in winds and should be considered when predicting landscape change.

Methods

M1. Extracting dune crests

Australian dune crests are extracted from the freely available Copernicus GLO-30 (COP30) digital surface model (DSM)[25], which has a horizontal resolution of 30 m at the equator (Extended Data Fig. 1b). We first calculate residual relief (RR) using a 20×20-pixel median filter (Extended Data Fig. 1c) and generate a binary dune outline map using a U-Net convolutional neural network trained to identify vegetated dunes[26,38]. The RR is then used to calculate volumetric obscurance (VO) within a 10-pixel radius (Extended Data Fig. 1d), with a vertical exaggeration of 1000 to enhance the detection of topographic crest lines[26,39]. VO values range from 0 to 1, with low and high values representing trough-like and crest-like topography, respectively. The VO is smoothed with a 3-pixel radius median filter to reduce small-scale noise and finally clipped by the dune outline map[26] (Extended Data Fig. 1d inset). A top-down skeletonization algorithm — adopted from the ‘Thin Greyscale Image to Skeleton’ QGIS plugin (https://github.com/havatv/qgisthingreyscaleplugin) — is applied to the clipped VO to extract crest lines[40]. The result depends on the VO threshold range, and therefore on the characteristics of the dune field and the intended application[26]. A narrow VO range (for example 1–0.9) generates more individual dune networks with fewer y-junctions, whereas a wider range (for example 1–0.1) retains more crest lines, producing fewer networks with more y-junctions. We use a VO range of 1–0.1 to maximize crest-line detection, particularly for the low-relief, laterally extensive linear dunes that characterize much of the Australian dune whorl. The resulting skeleton raster is thinned, vectorized and generalized using the ‘snakes’ algorithm in QGIS[26] (Extended Data Fig. 1e).

M2. Crest line cleanup

The low VO range and the 30-m resolution of the DSM can produce artificial connections between closely spaced crest lines, for instance across the interdune area between the upwind arms of a genuine y-junction. This produces repeated y- and multi-junctions and sometimes a ladder-like pattern. Such artefacts matter for signed orientation, because they can bias towards orientations set by the raster structure rather than the dune morphology. To reduce this bias, we identify all y- and multi-junctions, remove junction-associated crest segments shorter than 100 m and recalculate the junctions from the clean network. The 100-m threshold is based on the DSM resolution, as artificial connections typically consist

of two to three raster cells (about 60–90 m). This filter may also remove genuine short connections in closely spaced or multi-crested dunes. Visual inspection indicates that most removed features are artefacts, and we consider this trade-off preferable to retaining raster-induced orientation bias. The extracted crest lines and COP30 DSM are divided into 0.1°×0.1° analysis cells containing dunes (Extended Data Fig. 1a-e). We use the GEODATA TOPO 250K Series 3 'sand ridges' dataset from Geoscience Australia (https://pid.geoscience.gov.au/dataset/ga/64058) as an independent spatial mask to exclude cells outside mapped sand ridge areas. We then manually remove cells containing predominantly lake shorelines or mountain ranges that were misidentified as dunes (a consequence of the low VO range), as well as cells in which genuine dunes were outweighed by false-positive crest lines if the crest network is not representative of dune morphology. Removal of artificial junctions and non-representative cells from the masked crest lines results in < 2% loss of total whorl crest length. Finally, because of the resolution of the COP30, some subdued dunes (for example in the Barkly dune field[2]) lack the relief needed for our workflow and are not fully mapped.

M3. Dune crest orientation and slope

The cleaned crest lines (Methods M2; Extended Data Fig. 1e) are then used to derive a representative orientation for each 0.1°×0.1° cell containing dunes. Within each cell, crest lines are divided into 100-m segments, and the orientation of each segment is calculated. Because individual crest lines are unsigned, orientations are constrained to the range $-180° \le \theta < 0$, and their circular mean is calculated to obtain the mean unsigned crest orientation for each cell. To assign a downwind direction to this unsigned orientation, we use the y-junctions within each cell (Extended Data Fig. 1e,f). For each y-junction, we evaluate the orientations of all three arms within a 100-m radius. The smallest angle between two arms is taken as the junction opening, which points approximately upwind, and the bisector of this angle gives an estimate of the upwind direction. Bisector directions from all y-junctions in a cell are combined using a circular mean to obtain a representative upwind direction for the cell. We compare the mean upwind bisector with the mean unsigned crest orientation and, where necessary, add 180° to the unsigned crest orientation, giving a signed dune orientation α_{obs} of the cell pointing downwind. For cells at the margins of dune fields with too few y-junctions to determine a reliable direction, we assign an orientation manually (~18% of cells) from the orientations of neighbouring cells with sufficient y-junctions.

Because the crest lines are extracted from the COP30 DSM, they follow the underlying topography and can be used to derive topographic characteristics of the dunes. We sample each crest line at 100-m intervals and construct transects perpendicular to the local crest orientation (Extended Data Fig. 1e) to calculate the slope of the dune. To limit the inclusion of non-dune topography, we retain only transects bounded by neighbouring crest lines on both sides. We define the upper part of each dune as the elevation interval between the crest and half the relative height above the higher of the two adjacent troughs (Extended Data Fig. 1g). Linear regressions through the elevation data in this interval gives the slope angle on each side of the crest (Extended Data Fig. 1h). Left and right slopes are assigned relative to the mean signed dune orientation α_{obs} of the cell, so that the two sides are consistently defined when looking downwind along the crest. For each cell we calculate the median absolute slope $|S|$ from the average slope values of individual transects. Slope asymmetry ΔS is calculated for each transect as the left slope minus the right slope and summarized by its median across all transects in the cell. Positive ΔS therefore indicates steeper slopes on the left side of the crest, and negative ΔS steeper slopes on the right looking downwind (Fig. 3c, Extended Data Fig. 1i).

M4. Dune interaction and orientation variability

For each cell we construct 50 equally spaced transects perpendicular to the mean crest orientation and calculate the median crest spacing λ_{obs}. Crest lines are buffered by 10% of λ_{obs} and, together with multi-junctions and y-junctions, used to count the number of dune interactions n per cell. We calculate the dune interaction density I as[29]:

$$I = \frac{n}{A} \tag{1}$$

where A is the area of the cell (the circular analysis area). The non-dimensional interaction index I_* is[28] (Extended Data Fig. 2a):

$$I_* = I\lambda_{obs}^2 \tag{2}$$

We also calculate the circular standard deviation σ_{obs} of the segment orientations in each cell (Methods M3) as a measure of the variability of crest orientation (Extended Data Fig. 2b).

M5. Saturated sand flux from reanalysis winds

We use hourly 10-m zonal (u) and meridional (v) wind components (m/s) from the ERA5 reanalysis[22] for 1950–2025 to characterize the contemporary wind regime. ERA5-Land data[41] has a higher spatial resolution, but it systematically underestimates wind speeds relative to ERA5[42]. We therefore interpolate ERA5 winds (0.25°×0.25°) to 0.1°×0.1° grid cells (equivalent to the ERA5-Land grid), which is the resolution used throughout this study. For computational efficiency, hourly winds are binned by direction (128 bins from −180° to 180°, width 2.81°) and speed (128 bins from 0 m/s to 20 m/s, width 0.156 m/s). Wind speed u_z is calculated from u and v and converted to surface friction velocity u_* (m/s) with the logarithmic law of the wall:

$$u_* = \frac{u_z \kappa}{\ln\left(\frac{z}{z_0}\right)} \tag{3}$$

where κ is the von Kármán constant (0.41), z is the height above the surface (10 m for ERA5 winds) and z_0 is the aerodynamic roughness length. We use a common global value of z_0 = 10^{-3} m. To account for the speed-up of flow over dune topography[43], we use:

$$u_{*c}(\alpha) = u_*(1 + \delta|\sin(\theta - \alpha)|) \quad (4)$$

where $u_{*c}(\alpha)$ is the friction velocity at the dune crest. The sine term takes the angle between wind direction θ and crest orientation α into account, with winds perpendicular to the crest experiencing the strongest speed-up[43]. δ is the fractional speed-up factor defined as:

$$\delta = \beta\frac{H}{L} \quad (5)$$

with H being the dune height and L being the dune length. Assuming a triangular dune we use the absolute slope $|S|$ (Methods M3) to calculate the height over length ratio as $H/L = \tan(|S|)/2$. A value of β = 6 is commonly used for dunes on Earth so we calculate δ as $3\tan(|S|)$ for consistency with the literature[1]. The crest friction velocity is then used to calculate the saturated volumetric sand flux at the crest[44]:

$$Q = \begin{cases} C_Q\frac{u_{*t}\rho_f}{g\rho_s}({u_{*c}}^2 - {u_{*t}}^2) & if\ u_{*c} > u_{*t} \\ 0 & otherwise \end{cases} \quad (6)$$

where Q is the volumetric sand flux at the crest (m^2/s), C_Q is a dimensionless flux scaling parameter, u_{*t} is the surface friction threshold speed (m/s), g is gravitational acceleration (9.81 m/s^2), and ρ_f and ρ_s are fluid and sediment densities (kg/m^3). We use C_Q = 5, ρ_f = 1.2 kg/m^3 and ρ_s = 2650 kg/m^3. For this study we use the time-averaged flux q that we obtain by weighting Q by the number of hourly observations N from 1950 to 2025 ($q = \sum_N|Q|/N$). The flux is divided by 0.6 to account for the packing fraction of resting sand.

The threshold speed u_{*t} controls both direction and magnitude of sand transport and thus dune orientation. Rather than prescribing a single value, we evaluate 64 equally spaced threshold speeds between 0.01 m/s and 0.64 m/s (steps of 0.01 m/s) and calculate the corresponding sand flux, the dune elongation direction (Methods M8) and related the threshold speeds to vegetation cover (Methods M6).

Finally, to assess the directional variability of sand transporting winds for the Australian dune whorl we compute the ratio of the resultant drift potential (RDP) and the drift potential (DP) over a flat and unvegetated bed. To do so we use the friction velocity from Eq. 3 (no speed-up effect) assuming 200-µm quartz sand to obtain the threshold speed u_{*t0} and calculate the flatbed sand flux (Eq. 6 using u_* instead of u_{*c} and u_{*t0} for u_{*t}) and flux directionality[1,30] (RDP/DP; Extended Data Fig. 3). To calculate u_{*t0} we use[45]:

$$u_{*t0}(D) = \sqrt{A_N\left(\frac{\rho_p g D}{\rho_a} + \frac{\Gamma}{\rho_a D}\right)} \quad (7)$$

where A_N = 0.0123 and Γ = 1.65 x 10^{-4} kg/s^2, particle density ρ_p = 2650 kg/m^3, air density ρ_a =1.2 kg/m^3, g = 9.81 m/s^2 and D being the grain diameter[45–48].

To test whether a latitudinal shift of the modern wind regime could explain the spatial pattern of orientation variability, we cross-correlate the circular standard deviation of crest orientation (σ_{obs}; Extended Data Fig. 2b) with the flux variability (1-RDP/DP; Extended Data Fig. 3) evaluated at u_{*t0} at lags of up to ±4° in latitude and longitude. Missing values in both maps are filled by interpolation using a Gaussian filter (σ = 0.8°) before high-pass filtering by subtracting another Gaussian (σ = 1.5°). The cross-correlation is computed using fast Fourier transforms, excluding lags with fewer than 50% of the original (unfilled) overlapping cells. We take the lag with the highest absolute correlation as the shift that best aligns the two patterns.

M6. Fractional vegetation cover

We use the GEOGLAM Rangeland and Pasture Productivity (RaPP) dataset to infer modern vegetation cover[32]. RaPP provides monthly medians of photosynthetic (green), non-photosynthetic (brown) and bare-soil fractional cover at 500 m resolution, derived from 8-day composites of the MODIS Nadir BRDF-Adjusted Reflectance product (MCD43A4), collections 6 and 6.1. We combine the two collections into a continuous time series, resample total vegetation cover (photosynthetic plus non-photosynthetic) to the 0.1°×0.1° grid cells by spatial averaging and calculate the minimum vegetation cover over 2001 to 2025 for each cell (Fig. 2a; minimum, median and maximum cover for major dune fields in Extended Data Fig. 6a–c).

To relate fractional vegetation cover to threshold speed, we use the simplified formulation[31]:

$$u_{*t}(D, \lambda) = u_{*t0}(D)f_\lambda(\lambda) \quad (8)$$

where $u_{*t0}(D)$ is the threshold speed for a flat, dry and unvegetated surface for a given grain size D (Methods M5, Eq. 7), and $f_\lambda(\lambda)$ is a correction factor accounting for surface roughness[46,49]. Volumetric soil moisture, soil salt content and surface crust corrections are not explicitly included because suitable continent-wide datasets are unavailable, however their influence is likely implicitly incorporated in the field calibrated free parameters outlined below.

The surface roughness correction can be expressed as[46,49]:

$$f_\lambda(\lambda) = \left[(1 - \sigma_v m_v \lambda_v)(1 + \beta_v m_v \lambda_v)\left(1 - \sigma_s m_s \frac{\lambda_s}{1 - A_v}\right)\left(1 + \beta_s m_s \frac{\lambda_s}{1 - A_v}\right)\right]^{0.5} \quad (9)$$

where subscripts v and s denote vegetation and non-vegetation roughness elements, A_v is fractional vegetation cover, and λ_v and λ_s are the corresponding roughness densities. Because non-vegetation roughness density depends on land type and no continental dataset exists, we set λ_s = 0 (unless stated otherwise; Extended Data Fig. 6a–c), giving a simplified vegetation-only formulation:

$$f_\lambda(\lambda) = \sqrt{1 - \sigma_v m_v \lambda_v}\sqrt{1 + \beta_v m_v \lambda_v} \quad (10)$$

The vegetation roughness density is defined as[50]:

$$\lambda_v = -0.35 \ln(1 - A_v) \quad (11)$$

We use σ_v = 1.45, m_v = 0.16 and β_v = 202, and a constant grain diameter of 200 μm (unless stated otherwise) assuming quartz sand[46]. We apply Eq. 7–11 in two ways: In the forward direction, we calculate the modern minimum threshold speed $u_{*t,mod}$ for each cell from the minimum modern vegetation cover composite V_{mod} (the lowest vegetation cover for every cell from 2001 to 2025; Fig. 2a,d; minimum, median and maximum composite data for major dune fields are shown in Extended Data Fig. 6a–c). In the inverse direction, we solve Eq. 7–11 for A_v given the optimal threshold speed $u_{*t,opt}$ (Methods M8), using the smaller root of the quadratic in λ_v, to calculate optimal vegetation cover under which modern winds reproduce the observed dune orientations (Fig. 2b,e).

M7. Maximum threshold speed before sand flux shutdown

For each cell we calculate the maximum threshold speed $u_{*t,max}$ at which the ERA5 winds (1950–2025) still produce any flux. Because flux is 0 when $u_{*c} \leq u_{*t}$ (Methods M5, Eq. 6), $u_{*t,max}$ equals the highest crest friction velocity u_{*c} that occurs at least once in the 76-year hourly observations (Methods M5; Extended Data Fig. 4a). We convert $u_{*t,max}$ to the corresponding vegetation cover V_{max} using Eq. 7–11 (same assumptions as in Methods M5–M6; Extended Data Fig. 4b) and compare it with the minimum modern vegetation cover V_{mod} (Methods M6; Fig. 2a, Extended Data Fig. 4c).

M8. Elongation mode and optimal surface friction threshold speed

Dune orientation depends on the relative contributions of sediment transport, dune growth and migration. Where bed instability or dune migration dominates, dunes develop an orientation α_H associated with the maximum growth rate in height. In contrast, dunes developing on sediment-starved surfaces under bimodal or multidirectional wind regimes can elongate along an orientation α_E corresponding to the mean net sand transport direction without net migration[1]. Many Australian linear dunes extend for several kilometres with limited sediment in the interdune or from a localized sediment source, such as lunettes. We therefore assume that elongation is the dominant growth mechanism and that their orientation is best represented by α_E. Accordingly, we calculate α_E for each of the 64 threshold speeds for each cell containing dunes (Extended Data Fig. 5c). For a given u_{*t}, we test 128 dune orientations α (~3° bins) and calculate the along-crest $q_\parallel$ and across-crest $q_\perp$ components[1]:

$$q_\parallel = q\cos(\theta - \alpha) \quad (12)$$
$$q_\perp = q\sin(\theta - \alpha)$$

where θ is the wind direction and α is the dune orientation. The elongation mode α_E is the orientation at which the mean net across-crest flux is zero while the along-crest flux remains positive:

$$q_\parallel(\alpha_E) > 0 \text{ and } q_\perp(\alpha_E) = 0 \quad (13)$$

Because α_E varies with u_{*t}, we use the relationship between α_E and u_{*t} to find the optimal threshold speed $u_{*t,opt}$ for which α_E matches the observed signed dune orientation α_{obs} (Methods M1–M3). The optimal threshold speed $u_{*t,opt}$ is defined as the threshold speed of the intersection of $\alpha_E(u_{*t})$ and α_{obs} (Extended Data Fig. 5c). For multiple solutions of $u_{*t,opt}$, we select the lowest one unless $u_{*t,opt}$ < 0.2 m/s (approx. minimum threshold speed for Eq. 7 with listed parameters and $D \approx 80$ μm; Methods M5) in which case we use the next higher solution (~1.6% of cells use second solution, ~2.1% of cells remain with threshold speeds below 0.2 m/s).

M9. Net across-crest sand flux and surface friction threshold speed

The elongation mode α_E depends on u_{*t}, so a dune in equilibrium with the elongation mode ($\alpha_{obs} = \alpha_E$) at optimal threshold speed $u_{*t,opt}$ would be out of equilibrium if the threshold speed were to change ($\alpha_{obs} \neq \alpha_E$) unless the wind rose is perfectly invariant in speed. To quantify how the net mean across-crest flux would respond to a change in threshold speed, we fix the dune orientation at the observed value, which aligns with α_E at $u_{*t,opt}$, and evaluate the derivative of the net mean across-crest flux with respect to u_{*t} at the optimal threshold as:

$$\left.\frac{\partial q_\perp(\alpha_{obs})}{\partial u_{*t}}\right|_{u_{*t}=u_{*t,opt}} \quad (14)$$

Positive values of the derivative indicate that across-crest transport shifts to the left and negative values indicate a shift to the right side of the crest as u_{*t} increases (aligning with sign conventions in Methods M3). For better spatial comparison we report the direction of the change in net

mean across-crest flux relative to the dune crest orientation (90° to crest; Fig. 3e). The same analysis is also done for modern minimum threshold speeds $u_{*t,mod}$ — even though $\alpha_{obs} \neq \alpha_E$ for $u_{*t,mod}$ — to test this relationship for modern minimum vegetation (Fig. 3a,d; Extended Data Fig. 7).

M10. Sensitivity of the elongation mode to latitude and threshold speed

We calculate the sensitivity of the elongation mode α_E for a latitudinal wind shift ($\partial\alpha_E/\partial\phi$) and for a change in threshold speed ($\partial\alpha_E/\partial u_{*t}$). We calculate α_E from the same ERA5 winds for every cell but use the continent-wide median of all $|S|$ (Methods M5, Eq. 4–5) to keep δ fixed across cells so that $\partial\alpha_E/\partial\phi$ is not influenced by changes in dune geometry. To directly compare the influence of wind shift and threshold speed on dune orientation we consider a latitudinal shift of $\Delta\phi$ = 1.5° (from the literature[10]) and a threshold speed change of Δu_{*t} = 0.30 m/s (roughly equivalent to a 30% change in vegetation cover, a reasonable range based on modern vegetation cover). We use a constant continent-wide threshold speed of $u_{*tk} \approx 0.29$ m/s that has been used in earlier continental drift maps[9,10] at which we evaluate the sensitivities. Relative sensitivity is calculated as $(|\Delta\phi\partial\alpha_E/\partial\phi|/|\Delta u_{*t}\partial\alpha_E/\partial u_{*t}|)|_{u_{*t}=u_{*tk}}$ (Fig. 4c,f).

Lastly, to assess the stability of the elongation mode, we calculate the ratio of the growth rates of the elongation and bed-instability modes σ_E/σ_H defined as[1]:

$$\frac{\sigma_E}{\sigma_H} = \frac{|q_\perp|(\alpha_E)}{|q_\perp|(\alpha_H)} \quad (15)$$

where α_H is the orientation that maximizes the growth rate in height and α_E is the elongation mode. The ratio ranges from 0 to 1, and values above 0.6 (from simulations[37]) indicate that elongation is the dominant mode[1]. Extended Data Fig. 8 shows this ratio for the optimal threshold speeds.

Data availability

All input datasets are publicly available. The Copernicus GLO-30 digital surface model[25] is distributed by the European Space Agency through OpenTopography (https://doi.org/10.5069/G9028PQB). ERA5 reanalysis data[22] are available from the Copernicus Climate Data Store (https://doi.org/10.24381/cds.adbb2d47). The GEOGLAM Rangeland and Pasture Productivity (RaPP) fractional vegetation cover dataset[32] is available through (https://doi.org/10.4225/08/5848a3f19a7b3). The GEODATA TOPO 250K Series 3 sand ridges dataset is available from Geoscience Australia (https://pid.geoscience.gov.au/dataset/ga/64058). Crest lines and main dataset produced in this study are available on Zenodo (will be published with DOI during review).

Code availability

The python code to reproduce this study can be accessed on GitHub (will be published with DOI during review).

References

1. Courrech du Pont, S. et al. Complementary classifications of aeolian dunes based on morphology, dynamics, and fluid mechanics. *Earth-Science Reviews* 255, 104772 (2024).
2. Hesse, P. P. The Australian desert dunefields: formation and evolution in an old, flat, dry continent. In *Australian Landscapes* (eds Bishop, P. & Pillans, B.) 141–164 (Geological Society, London, Special Publications 346, 2010).
3. Wasson, R. J., Fitchett, K., Mackey, B. & Hyde, R. Large-scale patterns of dune type, spacing and orientation in the Australian continental dunefield. *Australian Geographer* 19, 89–104 (1988).
4. King, D. The sand ridge deserts of South Australia and related aeolian landforms of the Quaternary arid cycles. *Transactions of the Royal Society of South Australia* 83, 99–108 (1960).
5. Wopfner, H. & Twidale, C. R. Geomorphological history of the Lake Eyre Basin. In *Landform studies from Australia and New Guinea* (eds Jennings, J. N. & Mabbutt, J. A.) 119–143 (Australian National University Press, Canberra, 1967).
6. Jennings, J. N. A revised map of the desert dunes of Australia. *Australian Geographer* 10, 408–409 (1968).
7. Bowler, J. M. & Magee, J. W. Geomorphology of the Mallee region in semi-arid northern Victoria and western New South Wales. *Proceedings of the Royal Society of Victoria* 90, 5–21 (1978).
8. Brookfield, M. Dune trends and wind regime in Central Australia. in *Piedmont Plains and Sand-Formations in Arid and Humid Tropic and Subtropic Regions* (ed. Mensching, H.) 121-153 (Zeitschrift für Geomorphologie Supplementband 10, Schweizerbart, Stuttgart, 1970).
9. Kalma, J. D., Speight, J. G. & Wasson, R. J. Potential wind erosion in Australia: A continental perspective. *Journal of Climatology* 8, 411–428 (1988).
10. Nanson, G. C., Chen, X. & Price, D. M. Aeolian and fluvial evidence of changing climate and wind patterns during the past 100 ka in the western Simpson Desert, Australia. *Palaeogeography, Palaeoclimatology, Palaeoecology* 113, 87–102 (1995).
11. Sprigg, R. C. Stranded and submerged sea-beach systems of southeast South Australia and the aeolian desert cycle. *Sedimentary Geology* 22, 53–96 (1979).
12. Fitzsimmons, K. E. et al. Late Quaternary palaeoenvironmental change in the Australian drylands. *Quaternary Science Reviews* 74, 78–96 (2013).
13. Hesse, P. P. How do longitudinal dunes respond to climate forcing? Insights from 25 years of luminescence dating of the Australian desert dunefields. *Quaternary International* 410, 11–29 (2016).
14. Twidale, C. R. The study of desert dunes in Australia. In *History of Geomorphology and Quaternary Geology* (eds Grapes, R. H., Oldroyd, D. & Grigelis, A.) 215–239 (Geological Society, London, Special Publications 301, 2008).
15. Hesse, P. P. & Simpson, R. L. Variable vegetation cover and episodic sand movement on longitudinal desert sand dunes. *Geomorphology* 81, 276–291 (2006).
16. Hesse, P. P., Telfer, M. W. & Farebrother, W. Complexity confers stability: climate variability, vegetation response and sand transport on longitudinal sand dunes in Australia's deserts. *Aeolian Research* 25, 45–61 (2017).
17. Shumack, S., Fisher, A. & Hesse, P. P. Refining medium resolution fractional cover for arid Australia to detect vegetation dynamics and wind erosion susceptibility on longitudinal dunes. *Remote Sensing of Environment* 265, 112647 (2021).
18. Fisher, A. & Hesse, P. P. The response of vegetation cover and dune activity to rainfall, drought and fire observed by multitemporal satellite imagery. *Earth Surface Processes and Landforms* 44, 2957–2967 (2019).
19. Nanson, G. C., Chen, X. Y. & Price, D. M. Lateral migration, thermoluminescence chronology and colour variation of longitudinal dunes near Birdsville in the Simpson Desert, central Australia. *Earth Surface Processes and Landforms* 17, 807–819 (1992).
20. Rubin, D. M. Lateral migration of linear dunes in the Strzelecki Desert, Australia. *Earth Surface Processes and Landforms* 15, 1–14 (1990).
21. Bristow, C. S. et al. GPR surveys of vegetated linear dune stratigraphy in central Australia: evidence for linear dune extension with vertical and lateral accretion. In *Stratigraphic Analyses Using GPR* (eds Baker, G. S. & Jol, H. M.) 19–33 (Geological Society of America Special Paper 432, 2007).
22. Hersbach, H. et al. The ERA5 global reanalysis. *Quarterly Journal of the Royal Meteorological Society* 146, 1999–2049 (2020).
23. Courrech du Pont, S., Narteau, C. & Gao, X. Two modes for dune orientation. *Geology* 42, 743–746 (2014).
24. Gunn, A., East, A. & Jerolmack, D. J. 21st-century stagnation in unvegetated sand-sea activity. *Nature Communications* 13, 3670 (2022).
25. European Space Agency. Copernicus Global Digital Elevation Model. Distributed by OpenTopography (2024).
26. Daynac, J., Bessin, P., Pochat, S., Mourgues, R. & Shumack, S. A new workflow for mapping dune features (outline, crestline and defects) combining deep learning and skeletonization from DEM-derived data. *Geomorphology* 463, 109369 (2024).

27. Hesse, P. P. Sticky dunes in a wet desert: formation, stabilisation and modification of the Australian desert dunefields. *Geomorphology* 134, 309–325 (2011).
28. Marvin, M. C., Lapôtre, M. G. A., Gunn, A., Day, M. & Soto, A. Dune interactions record changes in boundary conditions. *Geology* 51, 947–951 (2023).
29. Day, M. & Kocurek, G. Pattern similarity across planetary dune fields. *Geology* 46, 999–1002 (2018).
30. Wasson, R. J. & Hyde, R. Factors determining desert dune type. *Nature* 304, 337–339 (1983).
31. Shao, Y., Ishizuka, M., Mikami, M. & Leys, J. F. Parameterization of size-resolved dust emission and validation with measurements. *Journal of Geophysical Research* 116, D08203 (2011).
32. Guerschman, J. P. & Hill, M. J. Calibration and validation of the Australian fractional cover product for MODIS Collection 6. *Remote Sensing Letters* 9, 696–705 (2018).
33. Nowatzki, M., Thomas, D. S. G. & Bailey, R. M. Analysing large-scale patterns of linear dune morphology and their environmental controls in the south-western Kalahari. Earth Surface Processes and Landforms 51, e70412 (2026).
34. Hesp, P., Hyde, R., Hesp, V. & Zhengyu, Q. Longitudinal dunes can move sideways. *Earth Surface Processes and Landforms* 14, 447–451 (1989).
35. Gunn, A. Formation and reorganization time scales of aeolian landscapes. *Geology* 51, 351–355 (2023).
36. Telfer, M. W., Radebaugh, J., Cornford, B. & Lewis, C. Long-wavelength sinuosity of linear dunes on Earth and Titan and the effect of underlying topography. *Journal of Geophysical Research: Planets* 124, 2369–2381 (2019).
37. Gao, X., Narteau, C., Rozier, O. & Courrech du Pont, S. Phase diagrams of dune shape and orientation depending on sand availability. *Scientific Reports* 5, 14677 (2015).
38. Shumack, S., Hesse, P. & Farebrother, W. Deep learning for dune pattern mapping with the AW3D30 global surface model. *Earth Surface Processes and Landforms* 45, 2417–2431 (2020).
39. Rolland, T. et al. Volumetric obscurance as a new tool to better visualize relief from digital elevation models. *Remote Sensing* 14, 941 (2022).
40. Putniņš, A. & Tveite, H. Extracting and visualising glacial ice flow directions from digital elevation models using greyscale thinning and directional trend analyses. *Computers & Geosciences* 147, 104677 (2021).
41. Muñoz-Sabater, J. et al. ERA5-Land: a state-of-the-art global reanalysis dataset for land applications. *Earth System Science Data* 13, 4349–4383 (2021).
42. Baas, A. C. Systematic under-representation of ERA5 10 m wind speeds in the ERA5-Land product undermines wind energy studies. *Applied Energy* 412, 127634 (2026).
43. Jackson, P. S. & Hunt, J. C. R. Turbulent wind flow over a low hill. *Quarterly Journal of the Royal Meteorological Society* 101, 929–955 (1975).
44. Martin, R. L. & Kok, J. F. Wind-invariant saltation heights imply linear scaling of aeolian saltation flux with shear stress. *Science Advances* 3, e1602569 (2017).
45. Shao, Y. & Lu, H. A simple expression for wind erosion threshold friction velocity. *Journal of Geophysical Research: Atmospheres* 105, 22437–22443 (2000).
46. Darmenova, K., Sokolik, I. N., Shao, Y., Marticorena, B. & Bergametti, G. Development of a physically based dust emission module within the Weather Research and Forecasting (WRF) model: assessment of dust emission parameterizations and input parameters for source regions in Central and East Asia. *Journal of Geophysical Research: Atmospheres* 114, D14201 (2009).
47. Kang, J.-Y., Yoon, S.-C., Shao, Y. & Kim, S.-W. Comparison of vertical dust flux by implementing three dust emission schemes in WRF/Chem. *Journal of Geophysical Research* 116, D09202 (2011).
48. Foroutan, H. et al. Development and evaluation of a physics-based windblown dust emission scheme implemented in the CMAQ modeling system. *Journal of Advances in Modeling Earth Systems* 9, 585–608 (2017).
49. Raupach, M. R., Gillette, D. A. & Leys, J. F. The effect of roughness elements on wind erosion threshold. *Journal of Geophysical Research: Atmospheres* 98, 3023–3029 (1993).
50. Shao, Y., Raupach, M. R. & Leys, J. F. A model for predicting aeolian sand drift and dust entrainment on scales from paddock to region. *Australian Journal of Soil Research* 34, 309–342 (1996).

Acknowledgements

We acknowledge the people of the Kulin Nations as the Traditional Owners of the lands on which this research was conducted. This research was undertaken with the assistance of the Australian Government through the National Computational Infrastructure (#NCMAS-2025-120 to A.G.) and the Australian Research Council (#DE240100552 to A.G.).

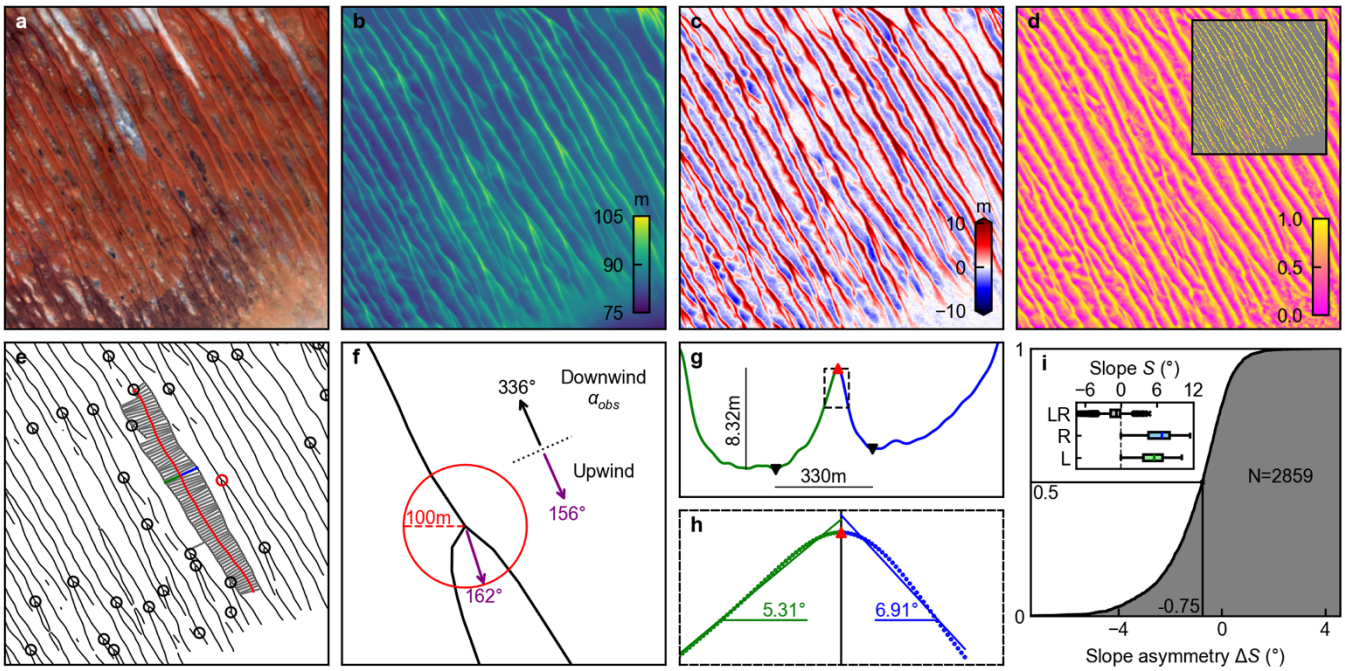
Ethics declaration

The authors declare no competing interests.

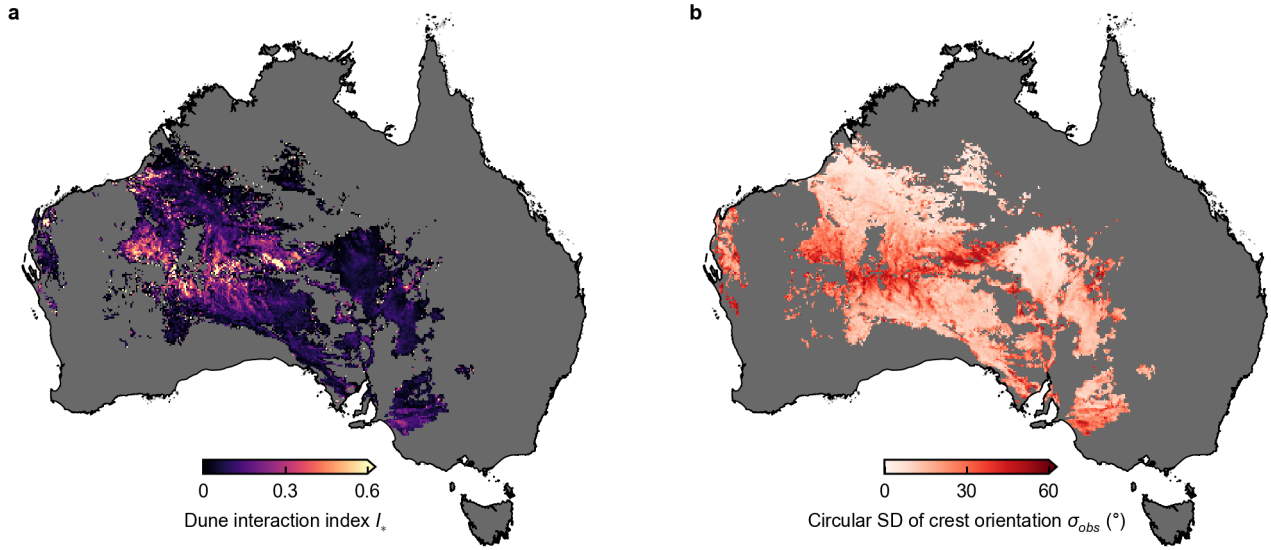
Author contributions

Formal analysis, Investigation, Validation, Visualization, Writing – Original Draft; DN. Data Curation; DN & JD. Conceptualization, Project administration; DN & AG. Methodology, Software, Writing – Review & Editing; all authors. Funding acquisition, Resources, Supervision; AG.

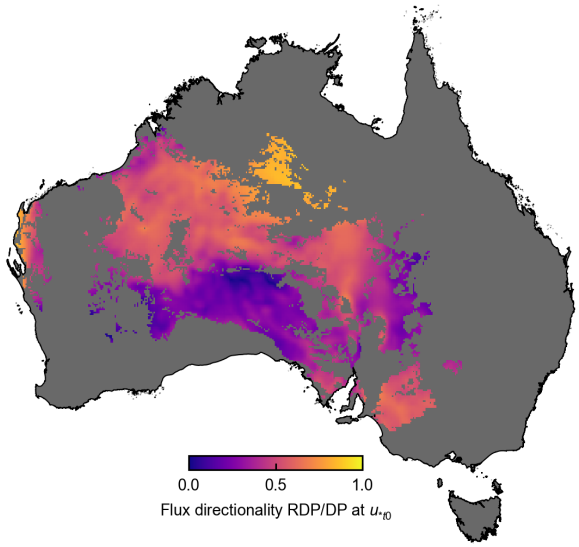
Extended Data



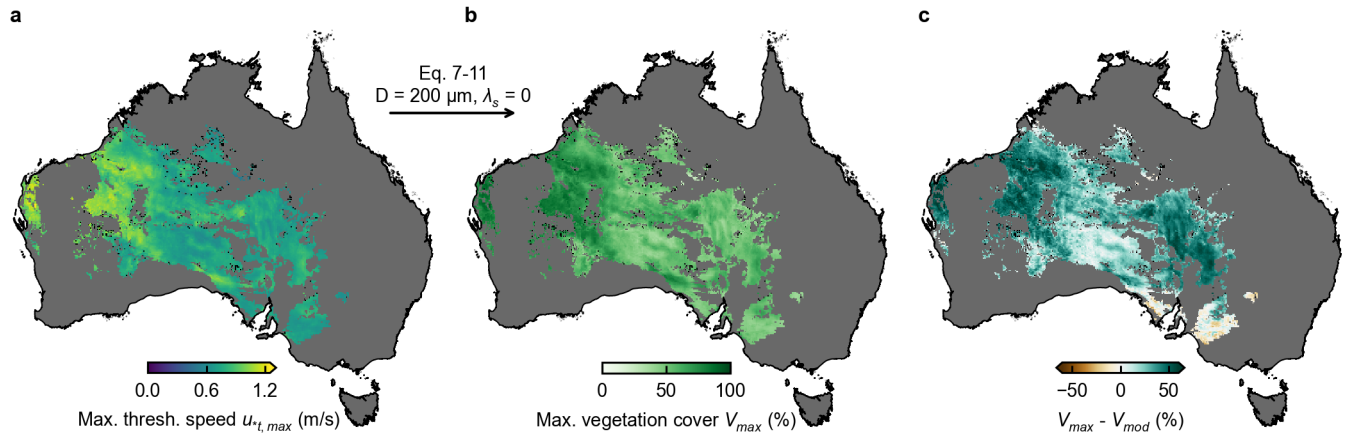
Extended Data Fig. 1: Workflow of extracting crest lines, orientation and slopes. a, Satellite imagery of a 0.1°×0.1° cell (137.9°, -24.7°). **b**, Topography from Copernicus GLO-30 DSM. **c**, Residual relief (RR) calculated from (b) using a 20×20 30-m pixel median filter. **d**, Volumetric obscurance (VO) calculated fro m (c) using a 10-pixel radius. Inset shows VO masked by dune outlines[26,38]. **e**, Crest lines (black) extracted from inset in (d) using a top-down skeletonization process[40] (Methods M1–M3). Example crest line in red with example transect left (green) and right (blue) looking downwind along the crest (northwest, see also g–i). Circles (black) show y-junction locations. Example y-junction is shown in red (see also f) and grey lines show transect spacing. **f**, Example y-junction of (e) with 100-m radius (red) and bisector (purple arrow in circle) of smallest opening angle pointing upwind. Average bisector direction (purple arrow; top right) for the whole cell shown in (e) used to sign the downwind (black arrow) direction of the unsigned cell circular average α_{obs}. Dotted black line is perpendicular to the crest to illustrate the upwind and downwind half (Methods M3). **g**, Across-crest transect left and right of dune crest extracted from the topography in (b). Black markers show troughs and red marker shows the crest. The view is downwind, in this case to the northwest (Methods M3). **h**, Upper part of the dune (dashed box in g) representing half the height between crest and shallower trough (here right side). Green and blue scatter points represent left and right side of the crest, respectively. Solid lines show linear interpolation used to obtain left and right slope angles (Methods M3). **i**, Cumulative histogram of slope asymmetry (left slope – right slope) for all transects in the example cell. Negative values represent steeper slopes on the right side of the crest. The median was chosen as a measure of slope asymmetry (here -0.75°). Box plots in the inset show left (L) and right (R) slopes as well as the slope asymmetries (LR) for all transects within the example cell (Methods M3).



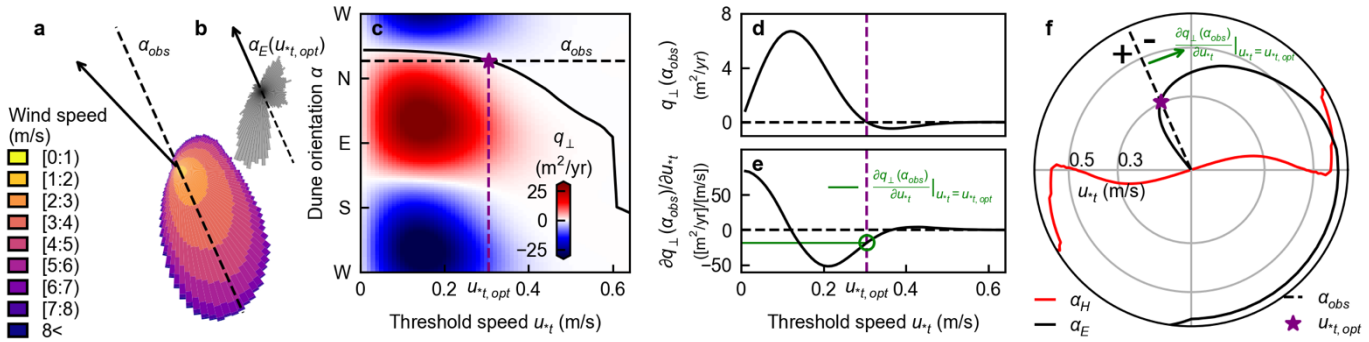
Extended Data Fig. 2: Dune interaction and orientation variability. a, Dune interaction index I_* per 0.1°×0.1° cell (Methods M4), a measure of changes in boundary conditions such as sediment availability, topographic confinement or wind regime[28]. **b**, Circular standard deviation σ_{obs} of crest orientation α_{obs}, showing areas of low and high variability in crest orientation (Methods M4).



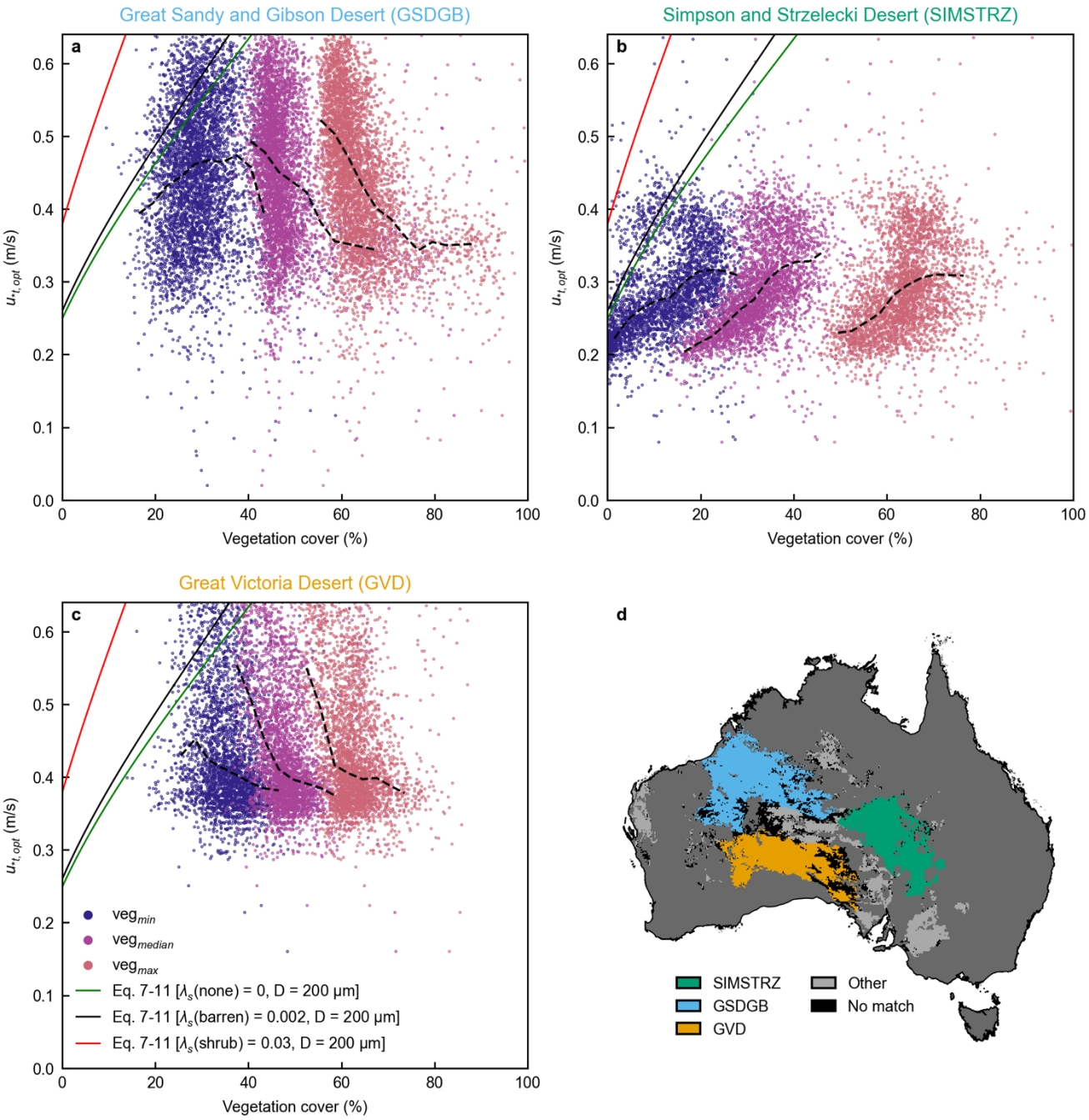
Extended Data Fig. 3: Flux directionality of sand-transporting winds for a bare bed. Ratio of resultant drift potential to drift potential (RDP/DP) evaluated at constant u_{*t0} ≈ 0.25 m/s assuming quartz sand of 200-μm diameter (Methods M5).



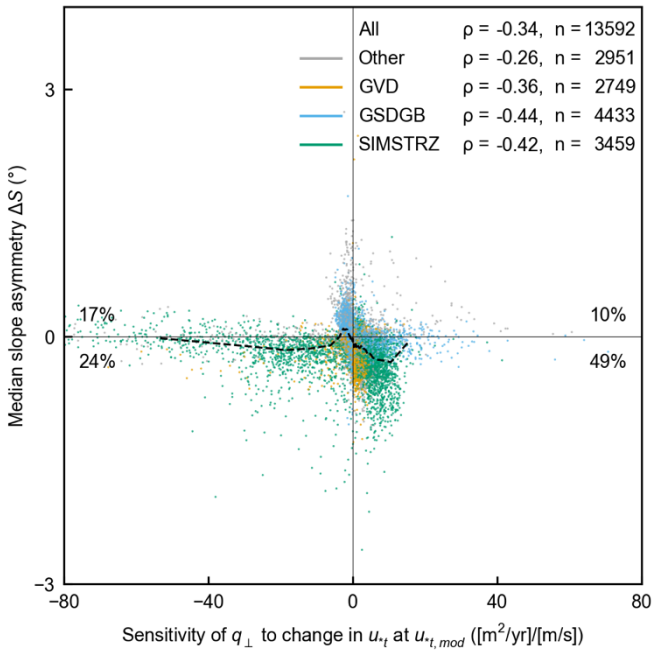
Extended Data Fig. 4: Modern minimum vegetation cover and sand flux shutdown. a, Maximum threshold speed $u_{*t,max}$ above which ERA5 winds (1950–2025) would produce no sand flux (Methods M6–M7). **b**, Vegetation cover V_{max} corresponding to $u_{*t,max}$ (a) for 200 µm sand (Methods M6). **c**, Difference between V_{max} and the minimum modern cover V_{mod} (Methods M6–M7, Fig. 2a). Brown: modern minimum vegetation would fully suppress sand flux. Green: modern minimum vegetation would still allow some flux for modern winds.



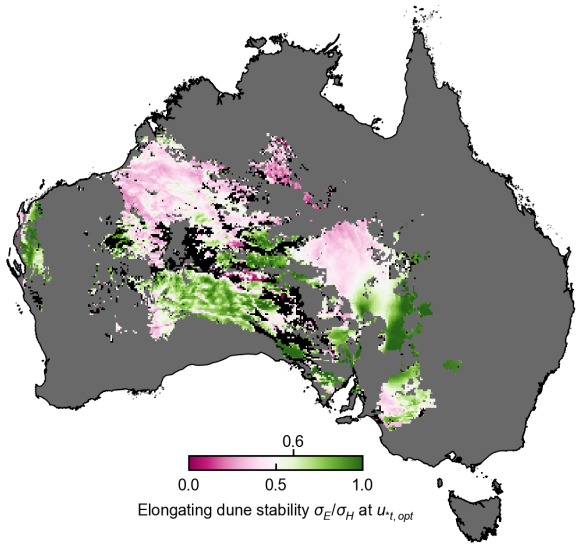
Extended Data Fig. 5: Workflow of sand flux modes as a function of surface friction threshold speed. a, ERA5 wind rose for the example cell (Extended Data Fig. 1) from 1950 to 2025 at 10 m height. **b**, Sand flux (Methods M5) of ERA5 winds (a) for the optimal surface friction threshold speed $u_{*t,opt}$ and observed dune orientation α_{obs}. **c**, Net across-crest sand flux $q_\perp$ over threshold speeds u_{*t} and dune orientations. The dashed line represents the observed dune orientation α_{obs} for the example cell while the solid black line represents the elongation mode α_E defined as $q_\parallel(\alpha_E) > 0$ and $q_\perp(\alpha_E) = 0$. The purple dashed line shows the optimal surface friction threshold speed $u_{*t,opt}$ that results in a match between observed orientation α_{obs} and the elongation mode α_E (Methods M8). **d**, Mean net across-crest sand flux $q_\perp(\alpha_{obs})$ over u_{*t} with $u_{*t,opt}$ (dashed purple line) resulting in $\alpha_E = \alpha_{obs}$. **e**, Sensitivity of $q_\perp(\alpha_{obs})$ to a change in surface friction threshold speed over u_{*t}. Green line shows rate of change evaluated at optimal surface friction threshold speed ($\partial q_\perp(\alpha_{obs})/\partial u_{*t}\,|_{u_{*t}=u_{*t,opt}}$). Negative or positive values indicate a shift in mean net across-crest flux to the right or left side of the dune, respectively, when surface friction threshold speed were to increase. **f**, Polar plot showing the observed dune orientation α_{obs} (dashed black line), the bed-instability mode α_H (red line), the elongation mode α_E (solid black line), the optimal surface friction threshold speed $u_{*t,opt}$ (purple marker) and the sign/direction of $\partial q_\perp(\alpha_{obs})/\partial u_{*t}\,|_{u_{*t}=u_{*t,opt}}$ (here negative; solid green arrow) as a measure of potential lateral dune migration/reorientation direction for an increase in u_{*t} (Methods M9).



Extended Data Fig. 6: Vegetation cover and optimal threshold speed by dune field. a–c, Optimal threshold speed $u_{*t,opt}$ against minimum (veg_{min}; equivalent to V_{mod}; Methods M6), median (veg_{median}) and maximum (veg_{max}) modern vegetation cover from Rangeland and Pasture Productivity (RaPP)[32] for the Great Sandy and Gibson deserts (GSDGB) (a), the Simpson and Strzelecki deserts (SIMSTRZ) (b) and the Great Victoria Desert (GVD) (c). Dashed black lines: trends for each composite. Solid black, red and green lines: relationship between vegetation cover and threshold speed for 200-µm sand with barren, shrub and no land-type-specific non-vegetation roughness density λ_s, respectively (Methods M6, Eq. 7–11). **d**, Location of the dune fields. Grey: cells with $u_{*t,opt}$ outside these deserts. Black: dune-containing cells without $u_{*t,opt}$.



Extended Data Fig. 7: Slope asymmetry over net across-crest flux sensitivity at modern minimum vegetation threshold. Median slope asymmetry ΔS (Methods M3) against the derivative of net across-crest sand flux $q_\perp$ with respect to u_{*t} (Methods M9), evaluated at the modern minimum vegetation threshold $u_{*t,mod}$, for each cell. Black dashed line shows the median trend (50 equal-count quantile bins). Spearman's ρ correlations are reported for the entire whorl and for individual dune fields (ρ and n refer to scatter points). Percentages in each quadrant give the share of scatter points falling in that quadrant. If a change in net across-crest flux causes slope asymmetry we'd expect clusters in the bottom left and top right quadrant. Values are only reported for cells that have an optimal threshold speed and where modern minimum thresholds produce sand flux (Fig. 3). Colours correspond to areas shown in Extended Data Fig. 6.



Extended Data Fig. 8: Elongation mode stability at the optimal threshold. Stability of elongating dunes σ_E/σ_H, from ERA5 winds (1950–2025) above the optimal threshold speed $u_{*t,opt}$ (Methods M10)[1]. Values above 0.6 indicate elongation stability in simulations[37].